Fast Single-Loop Voltage-Based MPPT Using Sliding-Mode Control for Switched-Inductor Multi-Cell Boost Converters

Reham Haroun, *Member, IEEE*, Abdelali El Aroudi, *Senior Member, IEEE*, Kuntal Mandal, *Member, IEEE*, Guidong Zhang, *Senior Member, IEEE*, Zhen Li, *Senior Member, IEEE*, and Luis Martínez-Salamero, *Life Senior Member, IEEE*

***Abstract*—A switched-inductor (SL) multi-cell boost converter is analyzed in this paper for a high-voltage gain application, stepping up a dc voltage from 36 V to 380 V in the first stage of a photovoltaic (PV) conversion chain. A fast maximum power point tracker (MPPT), processing the system input voltage, is used to extract the maximum power from the PV generator regardless of atmospheric conditions. A single sliding-mode control (SMC) loop forces the PV generator voltage to follow the maximum power point (MPP) voltage provided by a Perturb and Observe (P&O) algorithm. The sliding-mode analysis uses the equivalent control approach to demonstrate that the linearized ideal sliding dynamics are unconditionally stable. Theoretical predictions are corroborated by simulations and experimental measurements of the system under step-type changes in input irradiance and output load. The MPPT performance is experimentally evaluated against two classical approaches applied to a canonical boost converter: a current-based SMC and a voltage-based PWM. Both approaches track the MPP current and voltage, respectively, as given by the P&O algorithm. The proposed system outperforms the two classical systems, showing a better tracking accuracy.**

***Index Terms*—Photovoltaic, high gain dc-dc converter, MPPT, sliding-mode control, voltage-mode control.**

I. Introduction

FOSSIL fuel-based electrical energy is not only costly and limited but also has an adverse effect on the environment. For that reason, there is an increasing demand for the deployment of alternative sources of energy [1]. In this context, renewable energy sources (RESs) have proven to be a highly promising solution because of their vast utilization potential. This is the motive why nowadays RESs possess a measurable share in the global energy spectrum [2]. But the type and level of the output voltage/current of these renewable-based sources such as photovoltaic (PV) arrays, wind turbines, and fuel cells are not suitable for the direct connection to the ac mains, dc bus of a microgrid, battery system of an electric vehicle (EV), home appliances, etc. Due to this incompatibility, the scientific interest in power electronic converters continues to grow significantly, as they enable the integration of an increasing share of RESs with loads exhibiting diverse characteristics.

In this diversification of RESs, the utility-scale solar PV is the least costly option for new electricity generation. However, due to the wide difference between the voltage of a PV standard module (typically 30 V to 40 V) and the operating voltage of dc loads or dc buses (typically 380 V to 400 V), a high-voltage-gain dc-dc boost converter is required [3]. This kind of converters is also needed in many other applications such as in EV charging stations [4], microinverters [5], battery charging [6], data centers [7], satellites [8] and dc microgrids among others.

Designing a high-voltage gain dc-dc converter with a minimum number of components along with high efficiency and fast dynamic response is a challenging task. Several dc-dc converter topologies have been proposed and developed with a high voltage gain over the years [9]. Although theoretically, the conventional dc-dc boost converter could give a high voltage gain with high values of the duty cycle, in practice commercial pulse width modulators (PWM) do not operate properly beyond a duty cycle of 0.7. Nonetheless, a hysteretic comparator (HC) can work beyond the limit of 0.7 duty cycle at the expense of operating at the boundary between continuous conduction mode (CCM) and discontinuous conduction mode (DCM) to minimize the power losses caused by the parasitic parameters [10]. Cascaded boost converters [11], [12] can be used to mitigate this problem but at the price of a lower efficiency caused by multiple power processing stages.

On the other hand, high-voltage gain in a single stage can be achieved with high efficiency and few components

Received 7 November 2024; revised 15 February 2025 and 26 April 2025; accepted 18 July 2025. Date of publication 30 July 2025; date of current version 12 January 2026. This work was supported by Spanish Ministerio de Ciencia e Innovación through MICIU/AEI/10.13039/501100011033 and "European Regional Development Fund/European Union (ERDF/EU)" under Grant PID2023-150839OB-I00. The work of Reham Haroun was supported by the Ministerio de Ciencia e Innovación under Grant PID2021-124229NB-I00. The work of Kuntal Mandal was supported by the Agency for Management of University and Research (AGAUR) Grants through the Ministry of Research and Universities of the Government of Catalonia under Grant 2020 BP 00260. The work of Zhen Li was supported in part by the National Science Foundation of China under Grant 60904003, Grant 52002126, Grant 52177168, and Grant 6200304; and in part by Australian Research Council under Grant IC21010021. This article was recommended by Associate Editor M. Wang. *(Corresponding authors: Kuntal Mandal; Zhen Li.)*

Reham Haroun, Abdelali El Aroudi, Kuntal Mandal, and Luis Martínez-Salamero are with the Department d'Enginyeria Electrònica, Elèctrica i Automàtica, Universitat Rovira i Virgili, 43007 Tarragona, Spain (e-mail: reham.haroun@urv.cat; kuntal.mandal@urv.cat).

Guidong Zhang is with the School of Automation, Guangdong University of Technology, Guangzhou 510006, China.

Zhen Li is with the School of Automation, Beijing Institute of Technology, Beijing 100811, China (e-mail: zhenli@bit.edu.cn).

Digital Object Identifier 10.1109/TCSI.2025.3592025

© 2025 The Authors. This work is licensed under a Creative Commons Attribution 4.0 License.
For more information, see https://creativecommons.org/licenses/by/4.0/

introducing isolated magnetic devices. For instance, a high-frequency step-up transformer is used in dc-dc push-pull and flyback converters [13], [14]. However, involving a transformer increases the size and may lead to saturation effects. Coupled inductors have been employed in single-stage non-isolated converters as an alternative to these transformer-based converters [15], [16], [17], [18], but the leakage inductance associated to the magnetic coupling can cause a high-voltage spike across the switch. This impairs the efficiency and limits the effective duty cycle. The Z-source converter has also been proposed as an alternative for high voltage gain [19], but the low efficiency of this topology has limited its use in PV applications as reported in [20]. A family of single-switch PWM converters has also been presented in [21] to show better performance and efficiency over the Z-source converter. In addition, a single-stage single-phase dual-output hybrid converter has been introduced in [22] but with low efficiency. Non-isolated high-gain converters can also be achieved by integrating a dual boost converter with a switched-inductor (SL) structure [23]. A competitive example of an efficient transformer-less solution is the quadratic boost converter with high dc gain reported in [24], which can step up the voltage of a standard photovoltaic panel up to 400 V. More recently, a novel switched-inductor (SL) multi-cell boost converter has been proposed for high voltage gain applications [25], where the steady-state analysis has been performed.

On the other hand, MPPT control is essential in a PV system since it continuously adjusts the working point of the PV source and forces its operation at the maximum power point (MPP), hence increasing the efficiency. Among many MPPT algorithms such as the classical (perturb and observe (P&O), incremental conductance (IC)), those of intelligent type (fuzzy logic, neural networks), the optimization-based strategies like particle swarm optimization (PSO), grey wolf optimization (GWO), and the ones of hybrid composition (PSO-P&O, Fuzzy-PSO), the most used MPPT techniques are P&O and IC algorithms [26]. Some variants of these two algorithms are also used in mobile PV applications such as wearable technology and rooftop electric vehicles under fast changing atmospheric conditions [27], [28], [29]. The main advantage of the conventional P&O technique is its simplicity of implementation and excellent cost-effectiveness. In addition, no knowledge of the PV generator characteristics is required. At steady-state, this technique forces the PV generator to operate in a limit cycle in the vicinity of its MPP with a small oscillation around it characterized by the MPPT perturbation period T_{mppt} (or frequency f_{mppt}) and its corresponding perturbation amplitude Δ_{mppt}.

In this context, the sliding-mode control (SMC) [30] has been used to perform extremum seeking control (ESC) for MPPT in PV systems exhibiting accuracy of tracking and easy integration in the control of dc-dc switching converters [31]. The resulting algorithms are known as sliding-mode extremum seeking control (SM-ESC) and a representative description of their behavior can be found in [32], [33], [34], [35], and [36]. More recently, fast and accurate convergence in tracking the MPP is the result of using SMC with self-optimization in a PV system using a boost converter as a power interface to the load [37]. Structurally similar in terms of functional blocks to the previous work but different in terms of mathematical functions processing the tracking error, a conductance-based MPPT has been reported in [38] with a complete analytical description of its tracking process. A power versus conductance curve of the PV source is used to accurately track the MPP.

Different sliding surfaces can be used in SMC-based MPPT implementations but they all have in common the use of a reference provided by the MPPT algorithm. For instance, in [34], the sliding surface corresponds to the error between a reference signal and the input capacitor current, the goal being tracking the MPP while rejecting a 100 Hz frequency disturbance in the dc output of a boost converter connected to a single-phase inverter. The sliding surface in [35] uses a linear combination of input capacitor voltage and inductor current together with a reference signal in a boost converter to supply a dc load. Based on the power-current characteristics of the solar panel, the work in [36] employs a sliding surface in a single-ended primary inductor converter (SEPIC) that corresponds to the error between the input inductor current and the reference current given by an MPPT algorithm. In all cases, besides sensing the current and voltage of the panel for the P&O algorithm, it is necessary to use sensors for either inductor or capacitor current to form the sliding surface. Indeed, using these variables is the key point for guaranteeing a sliding-mode regime.

With the aim of extracting the maximum power from a standard solar panel stepping up its voltage from $30-36$ V to 380 V in one stage, this paper introduces a single-loop voltage-based MPPT using SMC (SLVB-SMC). The proposal is an SMC-based MPPT strategy for an SL 4-cell boost converter with a switching function determined solely by the error between the PV voltage and a reference signal generated by a P&O MPPT algorithm. The main antecedent of this report is the work published in [39], where it was shown by simulation that SL multi-cell boost converters are characterized by a fast dynamic response when used for PV maximum power point tracking (MPPT) with a PWM-based control strategy. The novelty presented here is the use of SMC instead of PWM and the experimental verification of the theoretical predictions. This proposal does not require sensing the inductor current in a clear-cut contrast with all existing SMC-based MPPT methods. This is because the sliding-motions can be directly induced using the PV panel voltage error with respect to the MPP voltage as sliding variable. This is a remarkable feature of the SL multi-cell boost converter, which is reported here for the first time. More specifically, the main contributions of this paper are as follows:

- A systematic method is established for the design of SMC-based MPPT controllers in SL multi-cell boost converters using a simple switching surface based on the PV panel voltage error. The study includes the stability analysis of the system for a general case of N cells.
- The resulting SLVB-SMC requires only two sensors to measure both current and voltage of the PV panel contrary to the existing current-based SMC for MPPT controllers

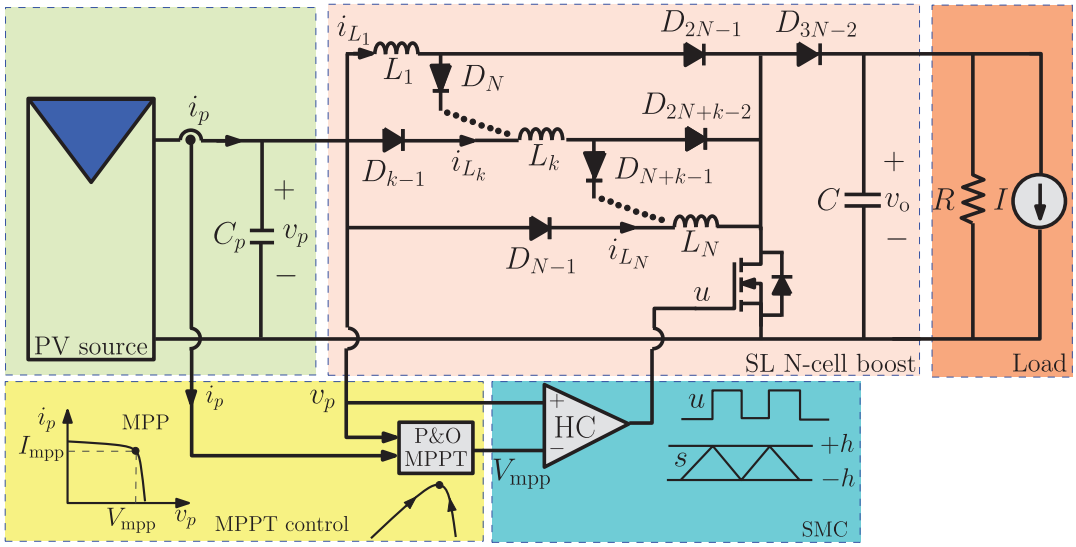


Fig. 1. Schematic circuit diagram of a PV fed SL $N-$cell boost converter loaded by CCL and resistor.

that require at least an additional sensor with a high bandwidth to measure an inductor current.

- The proposed SLVB-SMC yields a fast response to rapid changes of irradiance in the PV generator. It also produces fast stable transitions to new equilibrium points in response to step changes in the current load even in cases of absence of damping elements in the power stage.
- It exhibits less tracking error and small limit cycle amplitude around the MPP than classical SMC-based MPPT controllers processing the inductor current error with respect to the MPP current.
- In comparison with other SMC-based MPPT controllers, the method is simpler in terms of circuitry, which results in reduced hardware complexity and cost.

The remainder of the paper is organized as follows. Section II presents the system description and the mathematical modeling of the system consisting of a PV-fed multi-cell high-voltage-gain boost converter under an SLVB-SMC. The stability analysis is performed in Section III. Numerical simulations and experimental results are given in Section IV where the system's performance is evaluated. The experimental comparison of the proposed control with a current-based SMC and a voltage-based PWM for MPPT in a canonical boost converter is carried out in Section V. A discussion on the uniqueness of the proposal is given in Section VI. Finally, the conclusions of this work are summarized in the last section.

II. Description and Mathematical Modeling of the System

A. System Description

The system under study consists of a single PV generator that feeds a parallel combination of constant current load (CCL) and resistive load through an SL $N-$cell high voltage gain boost converter which was first proposed in [25]. Fig. 1 shows the schematic diagram of the described system. The SL $N-$cell boost converter acts as an interface between the PV generator and the load. A P&O MPPT control is used for generating the reference signal for the PV voltage which is controlled in such a way the PV source operates at the MPP. All the inductance values are considered identical for analysis simplicity, hence $L_1 = L_2 = \ldots = L$ which leads to equal corresponding inductor currents $i_{L_1} = i_{L_2} = \ldots = i_L$.

B. Full-Order Switched Model

By applying Kirchhoff's laws to the converter depicted in Fig. 1 and considering CCM, its dynamical behavior can be described by the following set of differential equations:

$$\frac{\mathrm{d}i_L}{\mathrm{d}t} = (1-u)\frac{v_p - v_o}{NL} + u\frac{v_p}{L} \tag{1a}$$

$$\frac{\mathrm{d}v_p}{\mathrm{d}t} = u\frac{i_p - Ni_L}{C_p} + (1-u)\frac{i_p - i_L}{C_p} \tag{1b}$$

$$\frac{\mathrm{d}v_o}{\mathrm{d}t} = (1-u)\frac{i_L}{C} - \frac{I}{C} - \frac{v_o}{RC} \tag{1c}$$

where $u \in \{0, 1\}$ is the discontinuous control variable for the converter.

The SL N-cell boost converter is controlled using an SMC by appropriately selecting its sliding variable according to the desired steady-state V_{mpp} of the PV voltage v_p. Namely, the sliding variable is selected as follows:

$$s = v_p - V_{\mathrm{mpp}} \tag{2}$$

where the reference voltage V_{mpp} is dictated by the MPPT control system.

The nature of the SMC is to operate ideally at an infinite switching frequency such that the controlled variable can track a certain reference to achieve the desired sliding-mode dynamic response and steady-state operation. However, infinite switching frequency operation is not possible due to the limited speed of the switching devices. In order to mitigate this problem, the switching policy is relaxed by using a hysteresis loop in the switching decision. This is achieved by the help of a HC. Accordingly, the switching frequency can be adjusted by the value of the hysteresis width h of the comparator.

C. Equivalent Control

The invariance condition of the sliding-mode regime to take place implies that $s = \dot{s} = 0$ [30]. Under this condition, the PV voltage v_p converges to its reference value, and an equivalent control input u_{eq} exists. This equivalent control corresponds to the system dynamics when the trajectory is confined into the switching surface defined by $v_p = V_{\text{mpp}}$, where the system switches with theoretically infinite frequency.

The expression of the equivalent control can be obtained by making $s = \dot{s} = 0$ and solving for u in the switched state equations [30]. For the SL $N-$cell boost converter, $\dot{s} = \frac{\mathrm{d}v_p}{\mathrm{d}t} = 0$. Now using (1b), the expression for the equivalent control is

$$u_{\text{eq}} = \frac{i_p - i_L}{(N-1)i_L} \tag{3}$$

Note that this equivalent control variable is not defined for the canonical boost converter ($N = 1$) with PV voltage as the controlled state variable. Hence, the SLVB-SMC of that converter is not possible. It should be pointed out that this variable must be bounded between the extreme values of the discontinuous binary variable u, i.e,

$$0 < u_{\text{eq}} < 1 \tag{4}$$

This range of the equivalent control can be used to determine the sliding-mode domain in the state space. The sliding-mode domain can be obtained by imposing the previous existence condition which results in a constrained range of the inductor current as follows:

$$\frac{i_p}{N} < i_L < i_p \tag{5}$$

Once more it can be observed that for a canonical boost converter ($N = 1$), this interval does not exist because it shrinks to a single point and sliding-mode regime will therefore not occur while for the SL $N-$cell boost converter, sliding-mode regime will take place once (5) is fulfilled.

D. Reduced-Order Model

Once the sliding-mode regime is reached and the system trajectory is confined into the switching surface defined by $v_p = V_{\text{mpp}}$, the system dynamical behavior can be described by a reduced-order dynamical model that can be obtained by substituting the discontinuous control input u by the equivalent control u_{eq} (3) in the switched model (1a)-(1c), and taking into account the order reduction imposed by the sliding condition $v_p = V_{\text{mpp}}$. The reduced-order ideal sliding dynamics model for the converter can be expressed as follows:

$$\frac{\mathrm{d}i_L}{\mathrm{d}t} = g_1(i_L, v_o) \tag{6a}$$

$$\frac{\mathrm{d}v_o}{\mathrm{d}t} = g_2(i_L, v_o) \tag{6b}$$

$$v_p = V_{\text{mpp}} \tag{6c}$$

where functions $g_1(\cdot)$ and $g_2(\cdot)$ are given by the following expressions:

$$g_1(i_L, v_o) = \frac{((N-1)V_{\text{mpp}} + v_{\text{o}})(i_p - i_L)}{NL(N-1)i_L} + \frac{V_{\text{mpp}} - v_{\text{o}}}{NL} \tag{7a}$$

$$g_2(i_L, v_o) = \frac{Ni_L - i_p}{(N-1)C} - \frac{I}{C} - \frac{v_o}{RC} \tag{7b}$$

This reduced-order model can be used for performing the stability analysis of the system under sliding-mode conditions.

III. Stability Analysis

By forcing $g_1(i_L, v_o) = 0$ and $g_2(i_L, v_o) = 0$, the equilibrium point can be calculated and it can be expressed as follows

$$\begin{pmatrix} I_L \\ V_o \end{pmatrix} = \begin{pmatrix} \dfrac{(I_{\text{mpp}} + (N-1)I)}{N} + \dfrac{(N-1)V_M}{2RN} \\ \dfrac{V_M}{2} \end{pmatrix} \tag{8}$$

where $V_M = \sqrt{R^2I^2 + 4RI_{\text{mpp}}V_{\text{mpp}}} - IR$ and we have considered that the PV generator is operated at the MPP as imposed by the MPPT control i.e., $i_p = I_{\text{mpp}}$. Using the expression of the equilibrium point given in (8), the steady-state value of the equivalent control (3) becomes:

$$U_{\text{eq}} = \frac{2R(I_{\text{mpp}} - I) - V_M}{2RI_{\text{mpp}} + (N-1)(2RI + V_M)} \tag{9}$$

In order to perform the stability analysis of the system, the nonlinear equations of the reduced-order model (7a)-(7b) are first linearized around the equilibrium point given in (8). Let $\hat{i}_L = i_L - I_L$ and $\hat{v}_o = v_o - V_o$. Then small-signal linearized model is given by

$$\begin{pmatrix} \dfrac{\mathrm{d}\hat{i}_L}{\mathrm{d}t} \\ \dfrac{\mathrm{d}\hat{v}_o}{\mathrm{d}t} \end{pmatrix} = \left(\begin{matrix} \dfrac{\partial g_1(i_L, v_o)}{\partial i_L} & \dfrac{\partial g_1(i_L, v_o)}{\partial v_o} \\ \dfrac{\partial g_2(i_L, v_o)}{\partial i_L} & \dfrac{\partial g_2(i_L, v_o)}{\partial v_o} \end{matrix} \right)\Bigg|_{(I_L, V_o)} \begin{pmatrix} \hat{i}_L \\ \hat{v}_o \end{pmatrix} \tag{10}$$

Therefore, after calculation of the different partial derivatives, the corresponding Jacobian matrix $\mathbf{J}$ is obtained and can be expressed as follows:

$$\mathbf{J} = \begin{pmatrix} \dfrac{2NR^2I_{\text{mpp}}(2(N-1)V_{\text{mpp}} + V_M)}{L(N-1)V_N^2} & \dfrac{2IR + V_M}{LV_N} \\ \dfrac{N}{(N-1)C} & -\dfrac{1}{RC} \end{pmatrix} \tag{11}$$

where V_N is given by

$$V_N = (N-1)(2RI + V_M) + 2RI_{\text{mpp}} \tag{12}$$

The characteristic polynomial of the Jacobian matrix $\mathbf{J}$ can be expressed as follows

$$P_J(\lambda) = \det(\lambda\mathbf{I} - \mathbf{J}) = \lambda^2 + \alpha\lambda + \beta \tag{13}$$

where $\mathbf{I}$ is 2×2 identity matrix and α, β are given by the following expressions

$$\alpha = \frac{(N-1)LV_N^2 + 2NCR^3I_{\text{mpp}}(2(N-1)V_{\text{mpp}} + V_M)}{(N-1)LCRV_N^2} \tag{14a}$$

$$\beta = \frac{N(V_MV_N + 2R(2(N-1)I_{\text{mpp}}V_{\text{mpp}} + IV_N + I_{\text{mpp}}V_M))}{(N-1)LCV_N^2} \tag{14b}$$

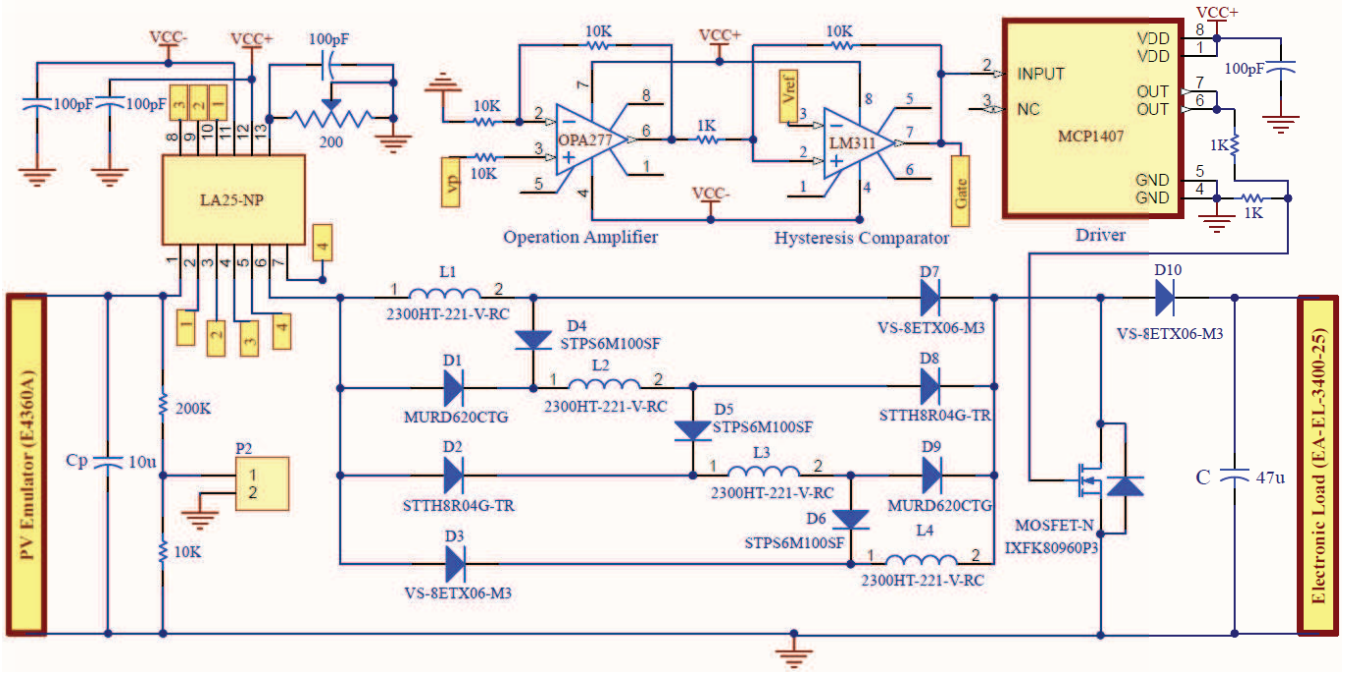


Fig. 2. The schematic circuit diagram of the prototype of PV-fed SL 4-cell boost converter loaded by a CCL.

Since $V_M > 0$ and $V_N > 0$, it can be observed that $\alpha > 0$ and $\beta > 0$ and therefore, the roots of the second-order characteristic polynomial (13) given in (15) are always located in the left half plane (LHP)

$$\lambda_{1,2} = -\frac{\alpha}{2} \pm \frac{1}{2}\sqrt{\alpha^2 - 4\beta} \tag{15}$$

Because $\sqrt{\alpha^2 - 4\beta} < \alpha$ as $\beta > 0$, the real part of the roots is always negative and consequently, the system is unconditionally stable.

It is worth noting that when the resistive load is not present ($1/R = 0$), see Fig. 1), the coefficients of the polynomial (13) become as follows

$$\alpha_{CCL} = \frac{NI_{mpp}V_{mpp}}{LI(N-1)(I_{mpp} + (N-1)I)} \tag{16a}$$

$$\beta_{CCL} = \frac{NI}{LC(N-1)(I_{mpp} + (N-1)I)} \tag{16b}$$

Since $\alpha_{CCL} > 0$ and $\beta_{CCL} > 0$, the system is also unconditionally stable in this case.

Unlike conditional stability, where stability depends on specific parameter values or operating conditions, unconditionally stable systems do not require fine-tuning of parameters to maintain stability. For a linear continuous system time-invariant (LTI) system, unconditional stability implies that all poles of the system's transfer function remain in the left half of the complex plane regardless of parameter variations.

IV. Numerical Simulations and Experimental Validation

In this section, the numerical simulations and the experimental measurements are presented to validate the previous theoretical results. The numerical simulations are performed using the circuit switched model implemented in the PSIM© software. It is worth noting that although in the previous theoretical analysis a resistive load together with a CCL was considered, in both the simulations and the experiments this resistive load has not been used. Note that this case is more challenging from a control point of view because ideally, the system does not have any damping element in the power stage.

The schematic circuit diagram of the experimental prototype is depicted in Fig. 2. The prototype was developed in the laboratory using two PCBs, one for the power stage and the other for the control. The SL 4−cell ($N = 4$) high-voltage-gain boost converter has been implemented using four identical toroid inductors. One MOSFET switch has been used. Ten diodes with different characteristics have been used to implement the SL and the main diode of the power stage. The SMC is implemented by analog control using operation amplifiers (OPA277) and a hysteresis comparator (LM311P). The reference signal for the PV generator voltage is provided by a P&O MPPT algorithm with perturbation period $T_{mppt} = 1$ ms ($f_{mppt} = 1$ kHz) and perturbation voltage $\Delta_{mppt} = 0.1$ V. The P&O MPPT algorithm has been implemented using a digital signal processor (DSP) chip (F2879D). The converter is loaded by a constant current load absorbing a current $I = 0.57$ A which is emulated by the electronic load EA-EL-3400-25. The input to the converter is fed by the PV emulator E4360A. In the simulation, the PV generator model TSM-340 has been used. The same parameters corresponding to the PV model are used in the PV emulator. A picture of the developed prototype in the laboratory with the measuring instruments is shown in Fig. 3. All the parameters for the power converter, controller, and PV generator are listed in TABLE I and TABLE II respectively.

From theoretical calculation using the set of parameter values shown in TABLE I and at an irradiance

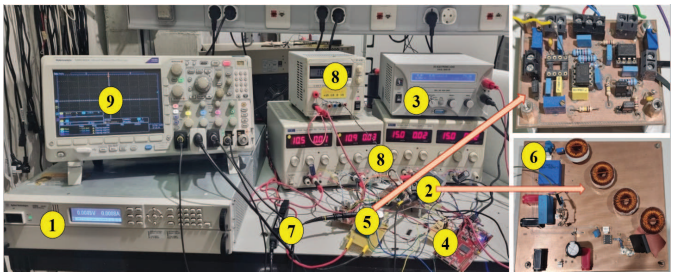


Fig. 3. A picture of the overall experimental setup. ① Solar array simulator E4360A, ② SL 4-cell boost converter power stage, ③ Electronic load EA-EL-3400-25, ④ DSP TMS320F28379D with the P&O MPPT control, ⑤ Analog voltage-based SMC, ⑥ PV current sensor LA25-NP, ⑦ current probe Tektronix TCP0030A (120 MHz), ⑧ Power supplies for driver, current sensor, analog and digital control and ⑨ Digital oscilloscope Tektronix MSO3014.

TABLE I

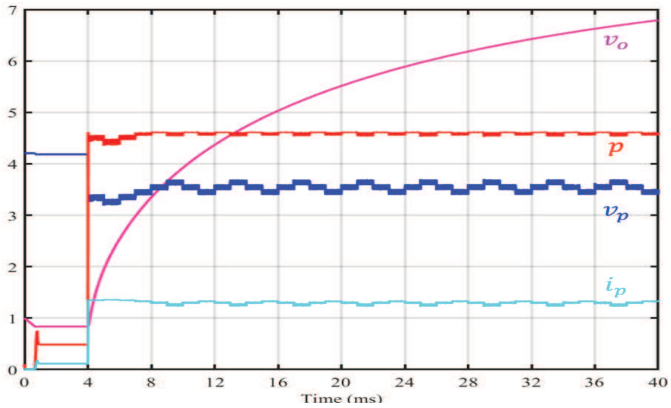
THE PARAMETER VALUES FOR SL 4-CELL BOOST CONVERTER

L	C_p	C	I	N	h	f_{mppt}	Δ_{mppt}
220 μH	10 μF	47 μF	0.57 A	4	1 V	1 kHz	0.1 V

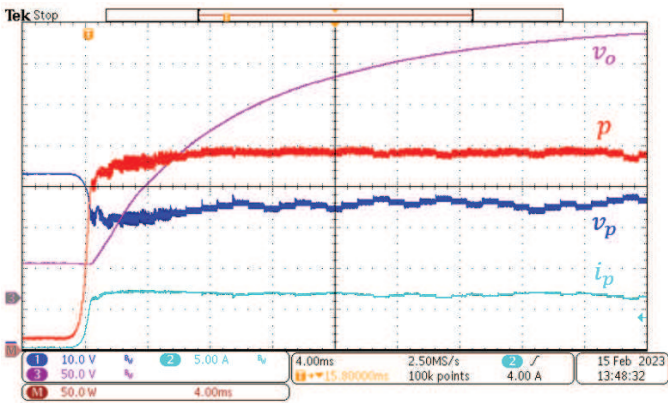
TABLE II

INTERNAL PARAMETER VALUES OF THE PV MODULE

Parameter	Value
Number of cells N_s	72
Standard light intensity S_n	1000 W/m^2
Ref temperature Θ_n	25^{o}C
Series resistance r_s	0.005 Ω
Parallel resistance R_p	1000 Ω
Short circuit current I_{sc}	7.67 A
Saturation current I_0	4.2×10^{-8} A
Band energy E_g	1.2 eV
Ideality factor A	1.3
Temperature coefficient C_Θ	0.00325 A/^{o}C



(a)



(b)

Fig. 4. The system response during the start-up at irradiance 900 W/m^2 and temperature $\Theta = 25^o$C. (a) Simulation, (b) Experimental. PV voltage (v_p) – 10 V/div, PV current (i_p) – 5 A/div, converter output voltage (v_o) – 50 V/div, and instantaneous power (p) – 50 W/div. Time base – 4 ms/div.

of 900 W/m^2, temperature Θ=25^{o}C, the switching frequency is $f_s = 61.64$ kHz [40] while experimentally, $f_s \approx 56$ kHz. The error can be attributed to parasitic elements and tolerances in the parameter values.

Fig. 4 shows the response of the system during start-up at an irradiance of 900 W/m^2, temperature $\Theta = 25^o$C. The waveforms of the voltage, current, and power of the PV emulator are illustrated. It can be noticed that the state variables at the input port of the system, where MPPT is performed, reach to steady-state in less than 4 ms. The output voltage takes more time to reach its steady-state. Note, however, that this variable is not regulated and that the time needed for reaching its steady-state depends on the output capacitance value. It can also be noticed that the PV source reaches its MPP in about four times the MPPT period $T_{\text{mppt}} = 1$ ms ($f_{\text{mppt}} = 1$ kHz), i.e, within 4 ms.

Fig. 5 shows the steady-state waveforms of the converter at an irradiance of 900 W/m^2 and temperature $\Theta = 25^o$C by numerical simulations and experimental measurements. In this figure, the voltage and the current of the PV source are illustrated. The extracted power is shown in the same figure where it can be noticed that the PV source is operating at the MPP corresponding to the used values of irradiance and temperature. In the same figure, it can be observed that the output voltage of the converter reaches 380 V, the PV voltage being about 36 V and hence the voltage gain of the converter is practically 11. Therefore, the numerical simulations and the experimental results are in good agreement. The measured efficiency for the SL 4−cell high-voltage-gain boost converter at this condition was 91%.

It is proved that the system is stable in the vicinity of the equilibrium point. The system is also tested under various parametric changes, including different irradiance levels and load variations, particularly when operating far from the equilibrium point. Firstly, a step change in irradiance level from 600 W/m^2 to 900 W/m^2 was carried out in the solar emulator and the resulting waveforms are shown in Fig. 6. It can be noticed that the transition from one MPP to another requires a small transient time of around 3 ms with a very small overshoot. Similarly, the output voltage requires a longer transient time to reach steady-state. The system trajectory in the $v_p - i_p$ plane under irradiance level change is shown in Fig. 7. It can be noticed that the system trajectory in the (v_p, i_p) plane moves from the operating point A at irradiance 600 W/m^2 to the other point B at irradiance 900 W/m^2 without any overshoot of the PV panel voltage v_p hence demonstrating the ability to control the PV generator voltage using a SLVB sliding-mode regime and forcing the system

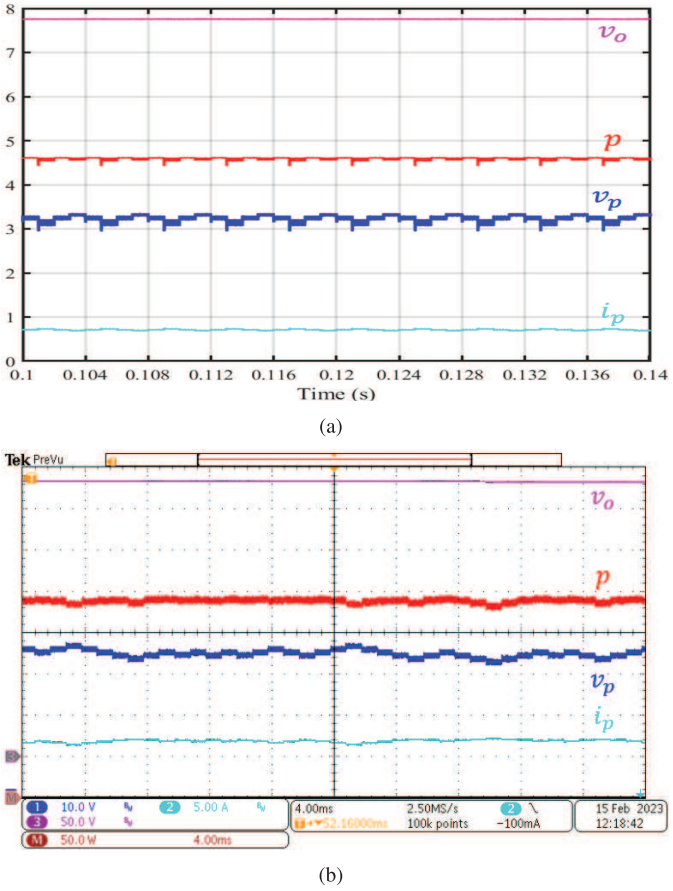


Fig. 5. The system response in the steady-state at irradiance 900 W/m^2 and temperature $\Theta = 25^o$C. (a) Simulation, (b) Experimental. PV voltage (v_p) – 10 V/div, PV current (i_p) – 5 A/div, converter output voltage (v_o) – 50 V/div, and instantaneous power (p) – 50 W/div. Time base – 4 ms/div.

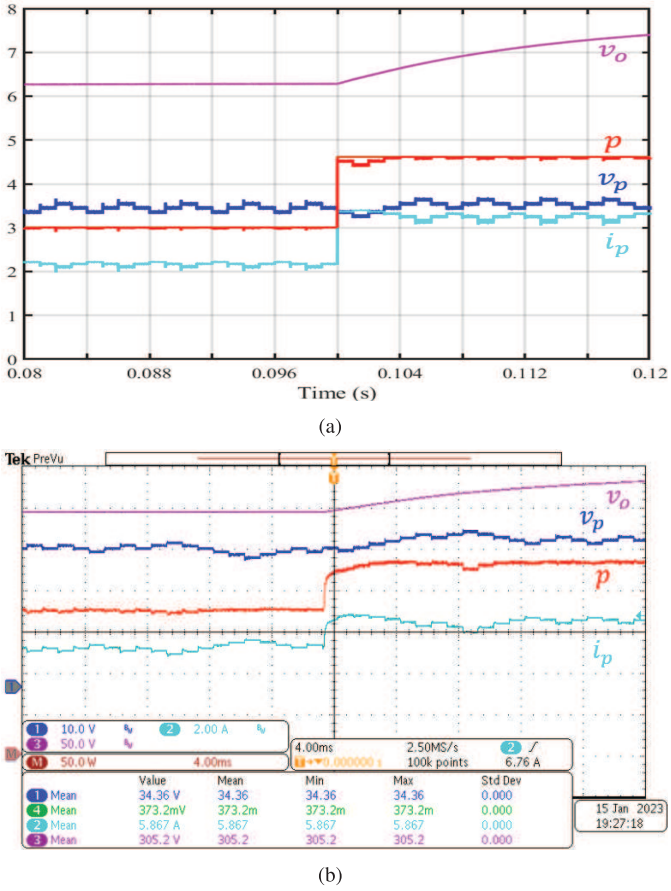


Fig. 6. The system response under step change in irradiance from 600 W/m^2 to 900 W/m^2 at temperature $\Theta = 25^o$C. (a) Simulation, (b) Experimental. PV voltage (v_p) – 10 V/div, PV current (i_p) – 2 A/div, converter output voltage (v_o) – 50 V/div, and instantaneous power (p) – 50 W/div. Time base – 4 ms/div.

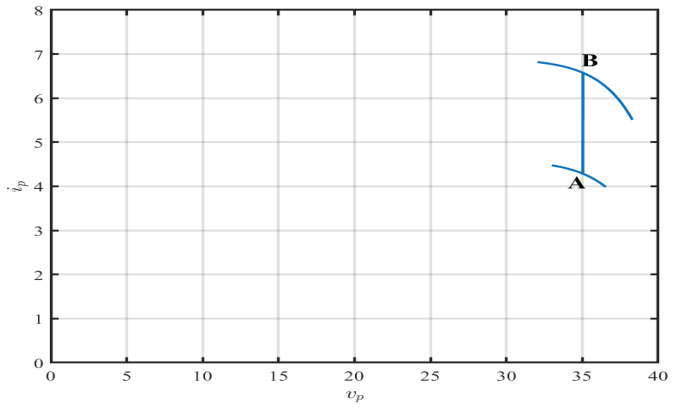
to operate in the vicinity of the MPP under external changes thanks to this control strategy.

The dynamic response of the SL 4−cell high-voltage-gain boost converter was also tested under a step change in the CCL current which was varied from 0.57 A to 0.8 A. The results are shown in Fig. 8 where the waveforms for the PV generator variables are illustrated. It is worth noting that the operating point has been adjusted to match the demanded power by the load. The output voltage of the converter decreases when the load current increases to maintain the power at the level dictated by the PV generator. In all the tests, a good matching can be observed between the numerical simulations and the experimental results. In terms of the response speed, the results reported in this paper outperform the ones reported in some key References using only voltage control to perform MPPT such as [41] where a boost converter performing a P&O MPPT, and the optimal selected MPPT perturbation frequency f_{mppt} was 100 Hz and [42] where the same converter was considered and the optimum selected perturbation frequency was 10 Hz for a motor pump application. In most studies employing the boost converter and the P&O MPPT method, the perturbation frequency does not exceed 100 Hz [34], [35], [37], [38]. In [34], both the capacitor current and the inductor current were utilized to enhance the system response speed, but this was at the price of increasing the number of current sensors and consequently the cost of the converter. In [36], the 500 Hz MPPT frequency using a SEPIC was reached thanks to the use of current mode control in sliding-mode operation.

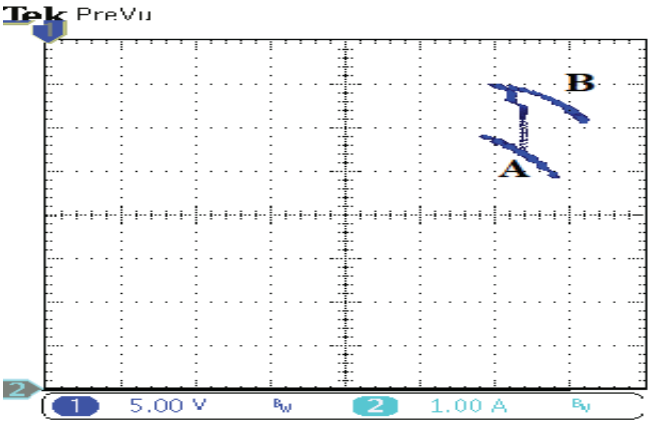
With the SL 4-cell boost converter, an MPPT frequency of 1 kHz was achieved, leading to a system response 10 times faster than the most of the reported works and 2 times faster than [36] without using any current feedback thanks to the fact that the topology allows voltage mode control in sliding regime. The results of the proposed system compared with some similar topologies have been summarized in Table III.

TABLE III
COMPARISON BETWEEN THE PROPOSED AND EXISTING APPROACHES

Reference	Converter	Current sensor	MPPT type	MPPT speed
[41]	Boost	Yes	P&O	100 Hz
[42]	Buck	Yes	P&O	10 Hz
[35]	Boost	Yes	P&O	50 Hz
[36]	SEPIC	Yes	P&O	500 Hz
[34]	Boost	Yes	P&O	16.6 Hz
[38]	quadratic boost	Yes	ESC	10 Hz
[11]	cascaded-Boost	Yes	ESC	100 Hz
[37]	Boost	Yes	Self-optimization	20 Hz
Proposed	SL N-cell boost	No	P&O	1 kHz

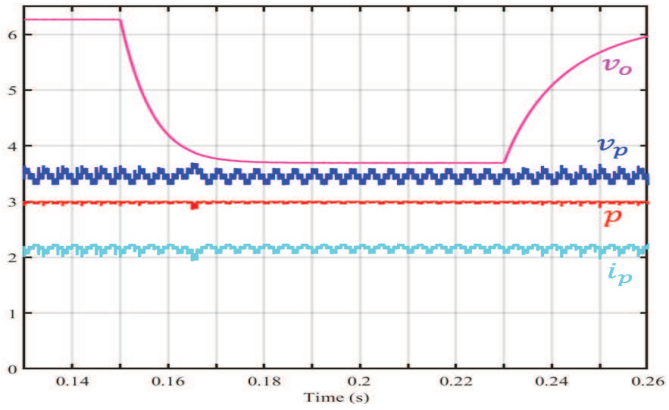


(a)

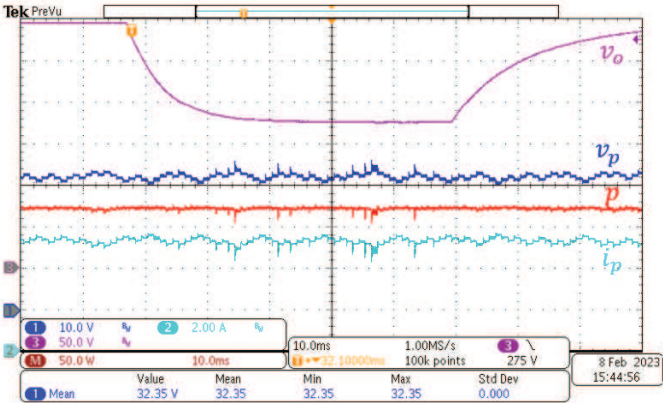


(b)

Fig. 7. Trajectories response under step change of irradiance from 600 W/m^2 to 900W/m^2 at temperature Θ = 25^{o}C. (a) Simulation, (b) Experimental. PV voltage (v_p) – 5 V/div, PV current (i_p) – 1 A/div.



(a)



(b)

Fig. 8. The system response under step change in the load from 0.57 A to 0.8 A at temperature Θ = 25^{o}C and irradiance 600 W/m^2. (a) Simulation, (b) Experimental. PV voltage (v_p) – 10 V/div, PV current (i_p) – 2 A/div, converter output voltage (v_o) – 50 V/div, and instantaneous power (p) – 50 W/div. Time base – 10 ms/div.

TABLE IV

THE PARAMETER VALUES FOR CURRENT-BASED SMC FOR MPPT OF A BOOST CONVERTER

L	C_p	C	I	h	f_{mppt}	Δ_{mppt}
220 µH	10 µF	10 µF	1.1 A	1.0 V	500 Hz	0.1 V

TABLE V

THE PARAMETER VALUES FOR VOLTAGE-BASED PWM FOR MPPT OF A BOOST CONVERTER

L	C_p	C	I	f_{PWM}	f_{mppt}	Δ_{mppt}
220 µH	10 µF	10 µF	1.1 A	50 kHz	500 Hz	0.1 V

V. COMPARISON OF THE PROPOSED APPROACH WITH TWO PREVIOUSLY REPORTED SOLUTIONS

This section provides a comparative analysis highlighting the advantages of the proposed control method. As mentioned in Section I, extensive research exists on high-gain conversion topologies. Here, the SL 4−cell boost converter with SLVB-SMC is compared with a canonical boost converter that uses current-based SMC and voltage-based PWM for MPPT control [11], [34] in two different cases, see Fig. 9. The parameter values are given in Table IV and Table V respectively. It should be noted that the SLVB-SMC for MPPT control is not feasible because the existing condition is not fulfilled.

Fig. 10 illustrates the experimental results for the start-up and steady-state regime of the boost converter under current- based SMC for MPPT, where the transient response is approximately 20 ms, which is significantly higher than the SL 4-cell boost converter. This slow response necessitates a longer perturbation time in the MPPT algorithm to ensure the system reaches a steady-state efficiently as shown by the steady-state response.

A step change in irradiance level from 600 W/m^2 to 900 W/m^2 was carried out in the solar emulator and the resulting waveforms are shown in Fig. 11. It can be noticed that the transition from one MPP to another requires a transient time of around 20 ms. As before, a larger transient time is required for the output voltage of the converter to reach the steady-state.

The system response under increased MPPT frequency f_{mppt} = 1 kHz is shown in Fig. 12. Note that a slow oscillation has started around the MPP and the waveforms of the variables are also oscillating.

Fig. 13 illustrates the experimental results for the start-up and steady-state regime of the boost converter under voltage-based PWM, where the transient response is approximately 50 ms, which is significantly higher than the SL 4-cell boost converter. This slow response necessitates a longer

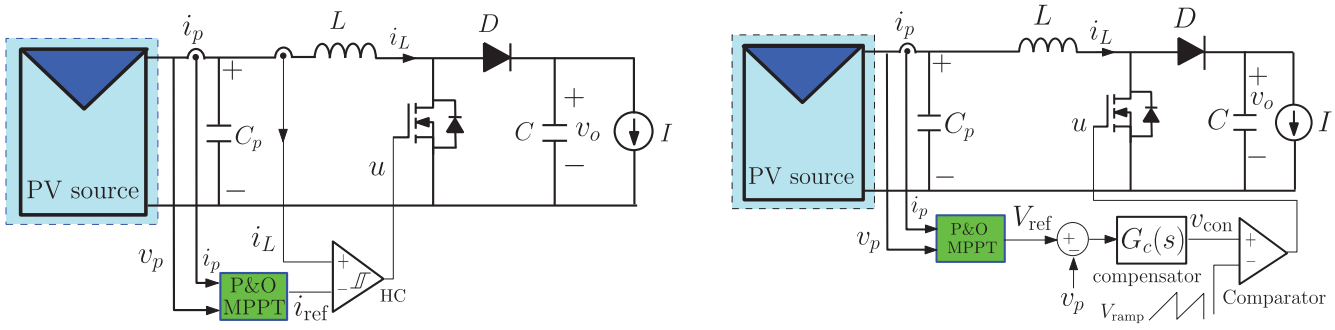


Fig. 9. Schematic circuit diagram of a PV fed boost converter loaded by CCL. (a) current-based SMC for MPPT control by means of hysteresis comparator (HC) (b) voltage-based PWM for MPPT.

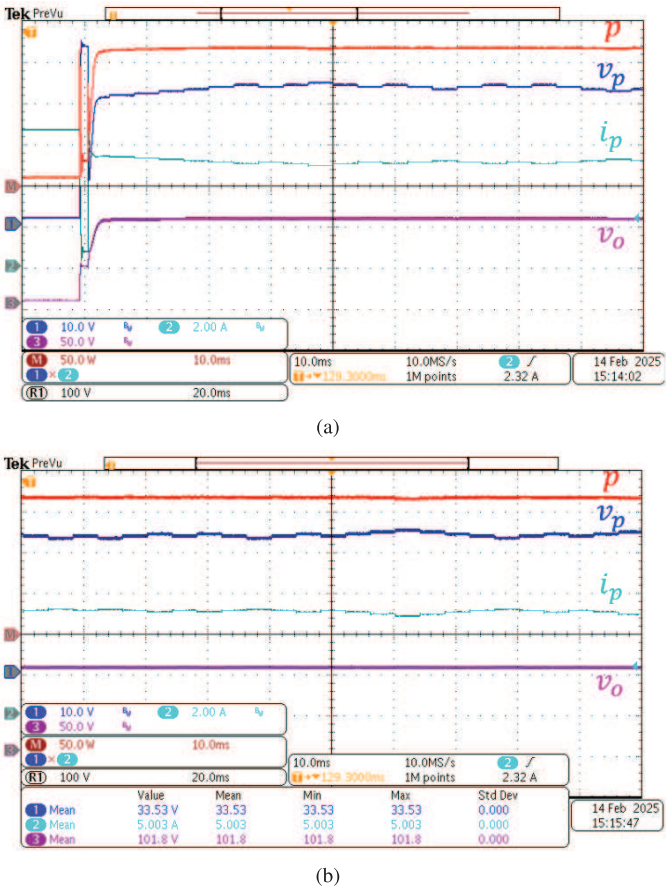


Fig. 10. The current-based SMC for MPPT of a boost converter response at irradiance 600 W/m^2 and temperature $\Theta = 25^o$C. (a) Start-up, (b) Steady-state. MPPT frequency $f_{mppt} = 500$ Hz. PV voltage (v_p) – 10 V/div, PV current (i_p) – 2 A/div, converter output voltage (v_o) – 50 V/div, and instantaneous power (p) – 50 W/div. Time base – 10 ms/div.

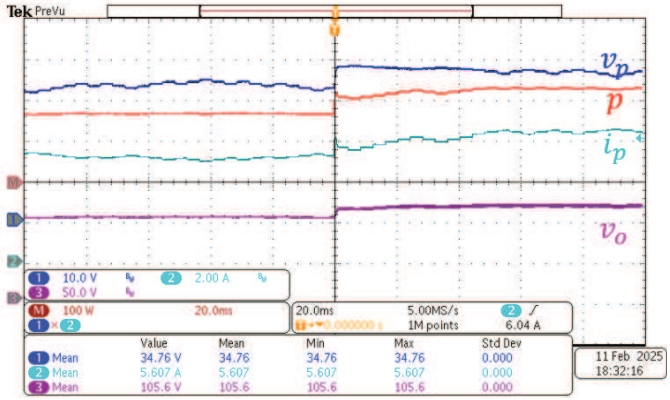


Fig. 11. The current-based SMC for MPPT of a boost converter response under step change in irradiance from 600 W/m^2 to 900 W/m^2 at temperature $\Theta = 25^o$C. MPPT frequency $f_{mppt} = 500$ Hz. Time base – 20 ms/div.

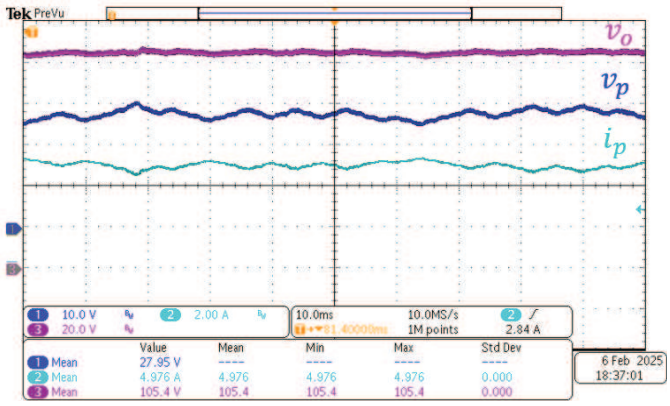
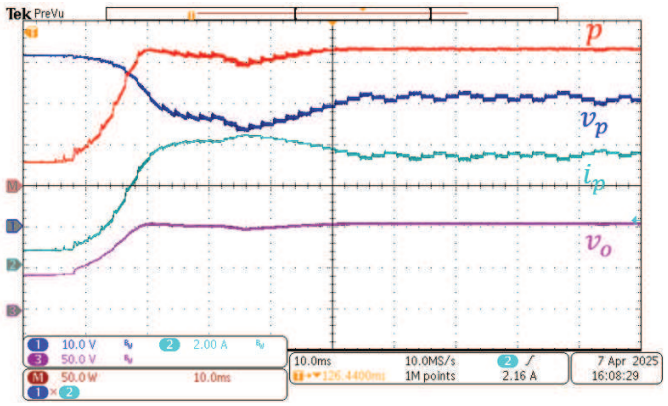


Fig. 12. The steady-state response of the current-based SMC for MPPT of a boost converter at irradiance 600 W/m^2 and and temperature $\Theta = 25^o$C. MPPT frequency $f_{mppt} = 1$ kHz. Time base – 10 ms/div.

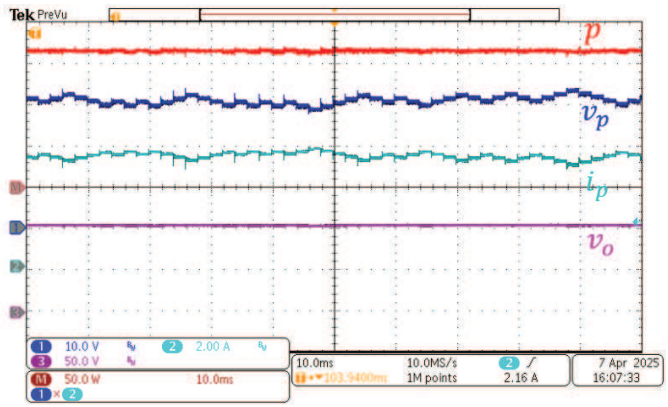
perturbation time in the MPPT algorithm to ensure the system reaches a steady-state efficiently as shown by the steady-state response.

A step change in irradiance level from 600 W/m^2 to 900 W/m^2 was carried out in the solar emulator and the resulting waveforms are shown in Fig. 14. It can be noticed that the transition from one MPP to another requires a transient time of around 30 ms. As before, a larger transient time is required for the output voltage of the converter to reach the steady-state.

To show the advantages of the proposed control method, a PV power profile (change in irradiance with time) is taken to compare the proposed control method with two other control methods for MPPT as shown in Fig. 15(a). From the results, it is clear that the SL 4-cell boost converter achieves a fast response (tracking the power profile) using SLVB-SMC. The



(a)



(b)

Fig. 13. The voltage-based PWM for MPPT of a boost converter response at irradiance 600 W/m^2 and temperature $\Theta = 25^o$C. (a) Start-up, (b) Steady-state. MPPT frequency $f_{mppt} = 500$ Hz. PV voltage (v_p) – 10 V/div, PV current (i_p) – 2 A/div, converter output voltage (v_o) – 50 V/div, and instantaneous power (p) – 50 W/div. Time base – 10 ms/div.

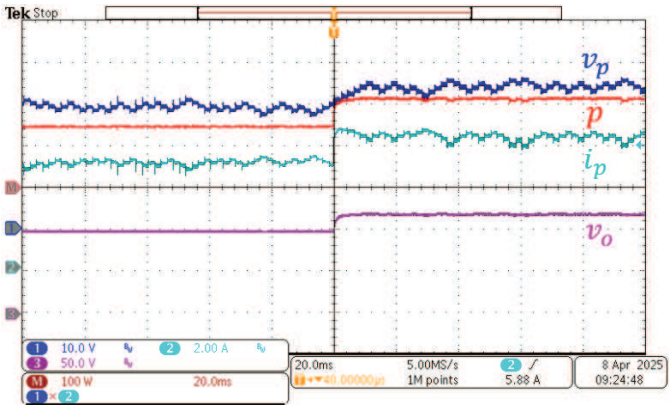
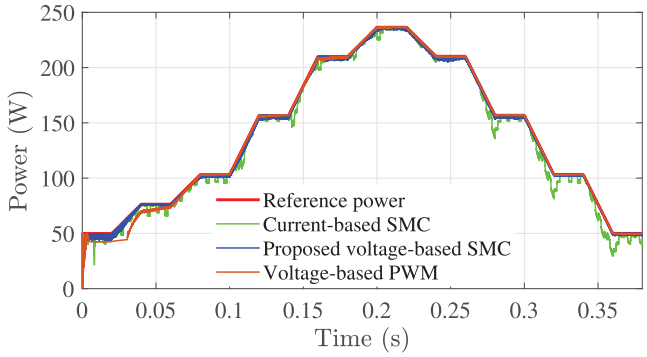


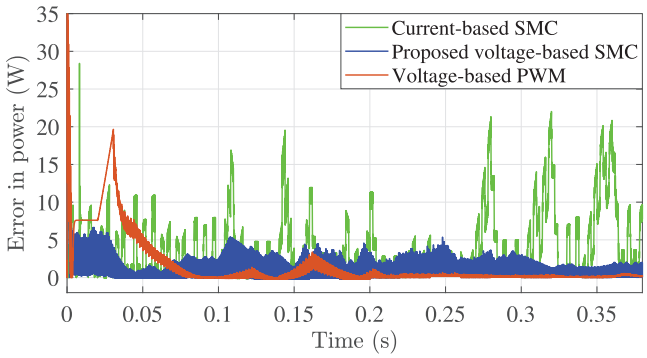
Fig. 14. The voltage-based PWM for MPPT of a boost converter response under step change in irradiance from 600 W/m^2 to 900 W/m^2 at temperature $\Theta = 25^o$C. MPPT frequency $f_{mppt} = 500$ Hz. Time base – 20 ms/div.

error (available PV power – MPPT power by control method) in power is shown in Fig. 15(b) where average power loss is higher in case of current-based SMC and voltage-based PWM for MPPT of boost converter. Therefore, average MPPT efficiency is higher in case of proposed SLVB-SMC.

The efficiency of the P&O MPPT mainly depends on two factors, namely perturbation frequency and perturbation



(a)



(b)

Fig. 15. (a) The PV power profile tracking performance by the three control methods. (b) The error in power (available PV power – MPPT power).

amplitude which depend on the converter topology and the control mode used. Therefore, these parameters can be selected based on the dynamic behavior of a specific converter as explained in [41]. As per the requirement, the perturbation frequency should be low enough to ensure that the system can reach a steady-state before the next perturbation occurs. However, if the PV-fed converter has a fast response, the perturbation frequency of the MPPT can be increased accordingly. The effects of these two parameters on the MPPT speed and the resulting tracking efficiency have been discussed in [42].

VI. Discussions: Uniqueness of the Proposal

This section discusses the peculiar feature of the SL multicell boost converters that allows the existence of sliding motions using the SLVB-SMC described above. We will show that other voltage step-up converters commonly used in PV applications cannot undergo sliding motions using the SLVB-SMC strategy but can reach the MPP using an SMC that processes a function of the input inductor current. The existence of sliding motions will be determined by vector analysis [43] and related to the scalar invariant conditions given by expression (3).

Converters in CCM can be described as follows

$$\dot{\boldsymbol{x}} = \boldsymbol{A}_1\boldsymbol{x} + \boldsymbol{B}_1 = \boldsymbol{f}_1(\boldsymbol{x}) \text{ for } u = 1 \tag{17a}$$

$$\dot{\boldsymbol{x}} = \boldsymbol{A}_0\boldsymbol{x} + \boldsymbol{B}_0 = \boldsymbol{f}_0(\boldsymbol{x}) \text{ for } u = 0 \tag{17b}$$

where $\boldsymbol{x}$ is the state vector. Equations (17) can be expressed in compact form as

$$\dot{\boldsymbol{x}} = \boldsymbol{A}_0\boldsymbol{x} + \boldsymbol{B}_0 + [(\boldsymbol{A}_1 - \boldsymbol{A}_0)\boldsymbol{x} + (\boldsymbol{B}_1 - \boldsymbol{B}_0)\boldsymbol{x}]\, u \tag{18}$$

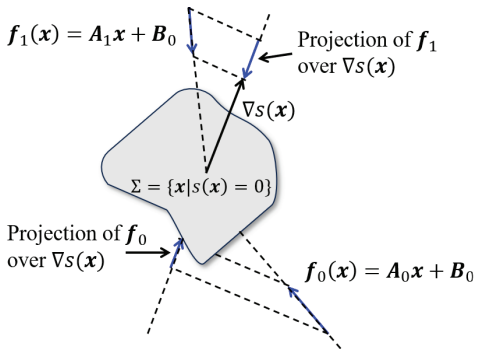


Fig. 16. Vector illustration of the existence of a sliding-mode [44].

TABLE VI
EQUIVALENT CONTROL FOR CONVERTERS OF FIG. 17

Topology	u_{eq} for SLVB	u_{eq} for SLCB
Boost	∄	$1-\frac{v_p}{v_C}$
Buck	$\frac{i_p}{i_L}$	$\frac{v_C}{v_p}$
Buck-Boost	$\frac{i_p}{i_L}$	$\frac{v_C}{v_C+v_p}$
Ćuk	∄	$1-\frac{v_p}{v_{C_1}}$
SEPIC	∄	$1-\frac{v_p}{v_{C_1}+v_{C_2}}$
Quadratic Boost	∄	$1-\frac{v_p}{v_{C_1}}$

Defining $\boldsymbol{A}=\boldsymbol{A}_0$, $\delta=\boldsymbol{B}_0$, $\boldsymbol{B}=\boldsymbol{A}_1-\boldsymbol{A}_0$, $\gamma=\boldsymbol{B}_1-\boldsymbol{B}_0$, the following bilinear description is obtained [44]

$$\dot{\boldsymbol{x}}=(\boldsymbol{A}\boldsymbol{x}+\delta)+(\boldsymbol{B}\boldsymbol{x}+\gamma)u=\boldsymbol{f}(\boldsymbol{x},u) \tag{19}$$

The existence of sliding motions can be illustrated as shown in Fig. 16 [44]. In that figure, ∇s is the gradient of the sliding surface while $\boldsymbol{f}_1(\boldsymbol{x})$ and $\boldsymbol{f}_0(\boldsymbol{x})$ represent respectively the vector field corresponding to $u=1$ (state vector trajectory above the switching surface) and $u=0$ (state vector trajectory below the switching surface). Sliding-mode exists when the projections of the field vectors $\boldsymbol{f}_1$ and $\boldsymbol{f}_0$ over the gradient ∇s are of opposite sign and pointed towards the switching surface defined by $\Sigma=\{\boldsymbol{x}|s(\boldsymbol{x})=0\}$. The conditions for the existence of a sliding-mode can be expressed as

$$\lim_{s\to 0^+}\langle\nabla s,\boldsymbol{f}_1(\boldsymbol{x})\rangle<0 \tag{20a}$$
$$\lim_{s\to 0^-}\langle\nabla s,\boldsymbol{f}_0(\boldsymbol{x})\rangle>0 \tag{20b}$$

where the notation $\langle a,b\rangle$ represents the scalar product of vectors a and b. The ideal sliding dynamics is characterized by an intermediate condition between (20) given by

$$s(\boldsymbol{x})=0 \tag{21a}$$
$$\langle\nabla s,\boldsymbol{f}(\boldsymbol{x},u_{eq})\rangle=0 \tag{21b}$$

Condition (21b) defines the equivalent control as the continuous function that constraints the system trajectory to $s(\boldsymbol{x})=0$. It can be expressed in scalar terms as $ds(\boldsymbol{x})/dt=0$, and hence equations (21a) and (21b) are called invariance conditions as mentioned above in Section II (subsection C). Condition (21b) can be also expressed as follows

$$\langle\nabla s,(\boldsymbol{A}\boldsymbol{x}+\delta)+(\boldsymbol{B}\boldsymbol{x}+\gamma)u_{eq}\rangle=0 \tag{22}$$

From (22) we derive the expression of the equivalent control

$$u_{eq}=-\frac{\langle\nabla s,(\boldsymbol{A}\boldsymbol{x}+\delta)\rangle}{\langle\nabla s,(\boldsymbol{B}\boldsymbol{x}+\gamma)\rangle} \tag{23}$$

Note that the equivalent control will exist if and only if

$$\langle\nabla s,(\boldsymbol{B}\boldsymbol{x}+\gamma)\rangle\neq 0 \tag{24}$$

Condition (24) is called transversality condition and implies that $\boldsymbol{B}\boldsymbol{x}+\gamma$ cannot be tangent to the switching surface [43].

Regarding the SL N-cell boost converter, equations (1) lead to the following matrices according to (17)

$$\boldsymbol{A}_1=\begin{pmatrix}0&0&\frac{1}{L}\\0&\frac{1}{RC}&0\\-\frac{1}{NC_p}&0&0\end{pmatrix},\ \boldsymbol{B}_1=\begin{pmatrix}0\\-\frac{I}{C}\\\frac{i_p}{C_p}\end{pmatrix},$$
$$\boldsymbol{A}_0=\begin{pmatrix}0&-\frac{1}{NL}&\frac{1}{NL}\\\frac{1}{C}&\frac{1}{RC}&0\\-\frac{1}{C_p}&0&0\end{pmatrix},\ \boldsymbol{B}_0=\begin{pmatrix}0\\-\frac{I}{C_p}\\\frac{i_p}{C_p}\end{pmatrix}$$

, the state vector being $\boldsymbol{x}=\begin{pmatrix}i_L\\v_o\\v_p\end{pmatrix}$, which results in $\boldsymbol{A}=\boldsymbol{A}_0$, $\boldsymbol{B}=\begin{pmatrix}0&\frac{1}{NL}&\frac{N-1}{NL}\\-\frac{1}{C}&\frac{1}{RC}&0\\-\frac{N-1}{C_p}&0&0\end{pmatrix}$, $\delta=\boldsymbol{B}_0$, and $\gamma\neq\boldsymbol{0}$.

For the switching variable $s(\boldsymbol{x})=v_p-V_{mpp}$, the corresponding gradient is $\nabla s=(0\ 0\ 1)$. From the calculated matrix expressions, $\boldsymbol{B}\boldsymbol{x}+\gamma$ can be expressed as follows

$$\boldsymbol{B}\boldsymbol{x}+\gamma=\left(\frac{v_p(N-1)+v_o}{NL}-\frac{i_L}{C}-\frac{(N-1)i_L}{C_p}\right)^{\intercal} \tag{25}$$

where the symbol $^{\intercal}$ stands for transpose operator.

Hence, $\langle\nabla s,(\boldsymbol{B}\boldsymbol{x}+\gamma)\rangle=-\frac{N-1}{C_p}\neq 0$, which justifies the existence of sliding-mode motion and equivalent control. In addition,

$$\boldsymbol{A}\boldsymbol{x}+\delta=\left(\frac{(v_p-v_o)}{NL}\quad\frac{i_L}{C}-\frac{v_o}{RC}-\frac{I}{C}\quad\frac{(i_p-i_L)}{C}\right)^{\intercal} \tag{26}$$

and finally from (23) the equivalent control expression in given by

$$u_{eq}=\frac{i_p-i_L}{(N-1)i_L} \tag{27}$$

which is exactly expression (3), that has been obtained above by means of the scalar description of the invariance conditions, i.e., $s(\boldsymbol{x})=0$ and $ds(\boldsymbol{x})/dt=0$.

If we reproduce the vector analysis in the converters depicted in Fig. 17, which are often used in PV applications, we deduce the results illustrated in Table VI. Two cases have been considered in the Table; namely, the switching variable $s(\boldsymbol{x})=v_p-V_{mpp}$, and the switching variable $s(\boldsymbol{x})=i_L-I_{mpp}$, in which i_L is the inductor current in buck, boost and buck-boost converters, and the input inductor current in Ćuk, SEPIC, and quadratic boost converters.

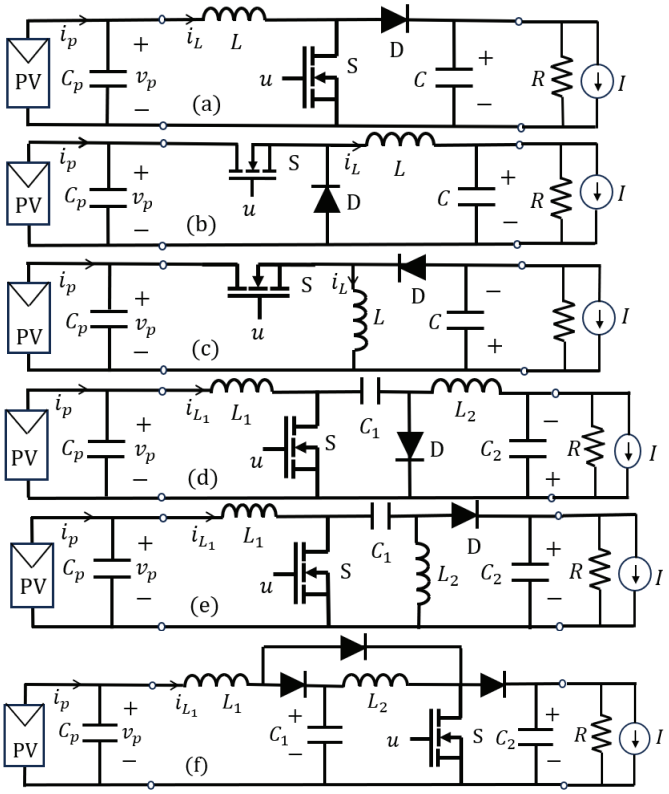


Fig. 17. Converters commonly used in the first stage of a PV conversion chain. (a) buck, (b) boost, (c) buck-boost, (d) Ćuk, (e) SEPIC, and (f) quadratic boost.

It can be observed in the table that there is no equivalent control and therefore no sliding-mode in the cases of the voltage step-up converters like boost and quadratic boost for the function $s(\boldsymbol{x}) = v_p - V_{\text{mpp}}$. Similar situation arises in Ćuk and SEPIC converters, which can be used as voltage step-up converters for duty cycles higher than 0.5. Conversely, there is sliding-mode along the switching surface in the case of the buck and buck-boost converters. Nonetheless, the buck converter is a voltage step-down circuit and the buck-boost converter could not be used here for voltage step-up applications because the resulting equivalent control $u_{\text{eq}} = i_p/i_L$ has an upper bound of 1, which implies that the inductor current i_L must be bigger than the panel current i_p, this case corresponding to a voltage step-down operation. Finally, it is worth mentioning that sliding-mode exists in all cases corresponding to single loop current-based (SLCB) $s(\boldsymbol{x}) = i_L - I_{\text{mpp}}$, which represents the foundation of the existing SMC-based MPPT methods mentioned in Section I.

The existence of equivalent control and consequently of sliding-mode in the cases of the SL N-cell boost, buck, and buck-boost converters when $s(\boldsymbol{x}) = v_p - V_{\text{mpp}}$ can be interpreted by considering the invariance condition $ds(\boldsymbol{x})/dt = 0$, which leads to

$$\frac{\mathrm{d}v_p}{\mathrm{d}t} = -\frac{i_L u_{\text{eq}}}{C_p} + \frac{i_p}{C_p} = 0 \quad \text{(buck and buck-Boost)} \tag{28}$$

$$\frac{\mathrm{d}v_p}{\mathrm{d}t} = -\frac{i_L(N-1)u_{\text{eq}}}{C_p} - \frac{i_L}{C_p} + \frac{i_p}{C_p} = 0 \quad \text{(SL N-cell)} \tag{29}$$

Expressions (28) and (29) show that the dynamics of the input voltage v_p is a function of the control variable u, and therefore the converters can be controlled in sliding-mode. On the contrary, the dynamics of the input voltage v_p results in the boost, Ćuk, SEPIC, and quadratic boost converters in the equation

$$\frac{\mathrm{d}v_p}{\mathrm{d}t} = -\frac{i_L}{C_p} + \frac{i_p}{C_p} \tag{30}$$

where i_L is the inductor current in the boost converter and the input inductor current in Ćuk, SEPIC, and quadratic boost converters. Note that equation (30) does not depend of the control variable u and hence the commutation resulting from $s(\boldsymbol{x}) > 0$ or $s(\boldsymbol{x}) < 0$ cannot induce sliding motions but other type of limit cycles when implemented with a hysteresis comparator.

The fact that the invariant condition $ds(\boldsymbol{x})/dt = 0$ leads straightforward in (28) to the equivalent control is a property of the proposed switching surface. It is said that the relative degree of the system for the selected surface is one because its first time derivative leads to the expression of the equivalent control [45].

VII. Conclusion

It has been shown in this paper that an SL $N-$cell boost converter is a competitive solution in the first stage of a PV chain requiring a high-voltage gain to step up a dc voltage from 36 V to 380 V. The reason of its competitive advantage lies in the simplicity of the MPPT system to extract the maximum power of the PV source irrespective of the atmospheric conditions. Unlike other converters used in PV voltage step-up applications, an SMC-based MPPT can be implemented in this converter with only two sensors to measure the current and voltage of the panel respectively. This is a significant benefit because the SMC-based MPPT does not need to measure an inductor current and therefore a high-bandwidth sensor system is not necessary.

The experimental results have demonstrated that the resulting tracking is faster than that of the reported works on the subject exhibiting a smaller tracking error when compared with that of either inductor current-based SMC or voltage–based PWM approaches.

Future work will consider a comparison on equal basis with a quadratic boost converter that takes into account the global efficiency of the PV chain, i.e. not only the MPPT efficiency but also the converter efficiency. Note that the quadratic boost converter requires an additional inductor current sensor for the SMC-based MPPT but it needs only 2 inductors, 2 capacitors and 3 diodes to step-up the voltage from 36 V to 380 V while the SL 4-cell boost converter necessitates 4 inductors, 1 capacitor and 10 diodes. The result of this comparison could establish the best solution for a voltage step-up single stage with a dc gain higher than 10 for PV applications.

References

[1] A. Qazi et al., "Towards sustainable energy: A systematic review of renewable energy sources, technologies, and public opinions," *IEEE Access*, vol. 7, pp. 63837–63851, 2019.

[2] (Jul. 18, 2025). *International Energy Agency*. [Online]. Available: https://www.iea.org/energy-system/renewables

[3] T. Sutikno, H. S. Purnama, N. S. Widodo, S. Padmanaban, and M. R. Sahid, "A review on non-isolated low-power DC–DC converter topologies with high output gain for solar photovoltaic system applications," *Clean Energy*, vol. 6, no. 4, pp. 557–572, Aug. 2022.

[4] R. Venugopal et al., "Review on unidirectional non-isolated high gain DC–DC converters for EV sustainable DC fast charging applications," *IEEE Access*, vol. 11, pp. 78299–78338, 2023.

[5] R. Hasan, W. Hassan, and W. Xiao, "PV microinverter solution for high voltage gain and soft switching," *IEEE J. Emerg. Sel. Topics Ind. Electron.*, vol. 3, no. 2, pp. 352–361, Apr. 2022.

[6] M. A. Mulla, V. J. Dobariya, R. V. Vamja, and A. Sircar, "Battery charger utilizing coupled inductor based high gain bidirectional DC–DC converter: Analysis, design, and implementation," *Eur. J. Electr. Eng.*, vol. 23, no. 3, pp. 175–184, Jun. 2021.

[7] P. T. Krein, "Data center challenges and their power electronics," *CPSS Trans. Power Electron. Appl.*, vol. 2, no. 1, pp. 39–46, Jul. 2017.

[8] A. Santoja, A. Barrado, C. Fernandez, M. Sanz, C. Raga, and A. Lazaro, "High voltage gain DC–DC converter for micro and nanosatellite electric thrusters," in *Proc. 28th Annu. IEEE Appl. Power Electron. Conf. Expo. (APEC)*, Mar. 2013, pp. 2057–2063.

[9] H. Tarzamni, H. S. Gohari, M. Sabahi, and J. Kyyrä, "Nonisolated high step-up DC–DC converters: Comparative review and metrics applicability," *IEEE Trans. Power Electron.*, vol. 39, no. 1, pp. 582–625, Jan. 2024.

[10] A. Leon-Masich, H. Valderrama-Blavi, J. M. Bosque-Moncusí, J. Maixé-Altés, and L. Martínez-Salamero, "Sliding-mode-control-based boost converter for high-voltage–low-power applications," *IEEE Trans. Ind. Electron.*, vol. 62, no. 1, pp. 229–237, Jan. 2015.

[11] R. Haroun, A. El Aroudi, A. Cid-Pastor, G. Garcia, C. Olalla, and L. Martinez-Salamero, "Impedance matching in photovoltaic systems using cascaded boost converters and sliding-mode control," *IEEE Trans. Power Electron.*, vol. 30, no. 6, pp. 3185–3199, Jun. 2015.

[12] R. Haroun, A. El Aroudi, A. Cid-Pastor, E. Vidal-Idiarte, H. Valderrama-Blavi, and L. Martinez-Salamero, "Modelling and control of modular DC-nanogrids based on loss-free resistors," *IEEE Access*, vol. 8, pp. 33305–33317, 2020.

[13] C.-T. Pan and C.-M. Lai, "A high-efficiency high step-up converter with low switch voltage stress for fuel-cell system applications," *IEEE Trans. Ind. Electron.*, vol. 57, no. 6, pp. 1998–2006, Jun. 2010.

[14] K.-B. Park, G.-W. Moon, and M.-J. Youn, "Nonisolated high step-up boost converter integrated with sepic converter," *IEEE Trans. Power Electron.*, vol. 25, no. 9, pp. 2266–2275, Sep. 2010.

[15] L. Schmitz, D. C. Martins, and R. F. Coelho, "Comprehensive conception of high step-up DC–DC converters with coupled inductor and voltage multipliers techniques," *IEEE Trans. Circuits Syst. I, Reg. Papers*, vol. 67, no. 6, pp. 2140–2151, Jun. 2020.

[16] S. Zhang et al., "A high-gain DC–DC converter with a wide range of output voltage," *Electronics*, vol. 12, no. 16, p. 3498, Aug. 2023.

[17] H. Hidalgo, R. Orosco, H. Huerta, N. Vázquez, C. Hernández, and S. Pinto, "A high-voltage-gain DC–DC boost converter with zero-ripple input current for renewable applications," *Energies*, vol. 16, no. 13, p. 4860, Jun. 2023.

[18] Y.-E. Wu, S.-C. Huang, and C.-M. Chang, "A novel single-switch high step-up DC–DC converter with high-voltage conversion ratio," *IEEE Trans. Circuits Syst. I, Reg. Papers*, vol. 72, no. 2, pp. 953–962, Feb. 2025.

[19] M. A. Ismeil, A. Francees, and R. Kennel, "Controller design for improved switched inductor (SL) Z-source inverter for photovoltiac applications," *Int. J. Renew. Energy Res.*, vol. 1, no. 5, pp. 345–353, Jul. 2012.

[20] A. E. Aroudi, R. Haroun, A. Cid-Pastor, A. Kouzou, and L. Martínez-Salamero, "A comparison between static and dynamic performances of a Z-source and a dual-stage boost converter under SMC for PV energy applications," *Energy Proc.*, vol. 42, pp. 587–596, Nov. 2013.

[21] E. H. Ismail, M. A. Al-Saffar, A. J. Sabzali, and A. A. Fardoun, "A family of single-switch PWM converters with high step-up conversion ratio," *IEEE Trans. Circuits Syst. I, Reg. Papers*, vol. 55, no. 4, pp. 1159–1171, May 2008.

[22] S. Prakash Sonkar, D.-C. Lee, and H. Cha, "A novel single-stage single-phase dual-output hybrid converter," *IEEE Trans. Circuits Syst. I, Reg. Papers*, vol. 71, no. 12, pp. 6385–6395, Dec. 2024.

[23] A. S. Mansour, A.-H.-H. Amer, E. E. El-Kholy, and M. S. Zaky, "High gain DC/DC converter with continuous input current for renewable energy applications," *Sci. Rep.*, vol. 12, no. 1, pp. 1–22, Jul. 2022.

[24] O. López-Santos, L. Martinez-Salamero, G. García, H. Valderrama-Blavi, and D. O. Mercuri, "Efficiency analysis of a sliding-mode controlled quadratic boost converter," *IET Power Electron.*, vol. 6, no. 2, pp. 364–373, Feb. 2013.

[25] G. Zhang et al., "Unique modular structure of multicell high-boost converters with reduced component currents," *IEEE Trans. Power Electron.*, vol. 33, no. 9, pp. 7795–7804, Sep. 2018.

[26] T. Esram and P. Chapman, "Comparison of photovoltaic array maximum power point tracking techniques," *IEEE Trans. Energy Convers.*, vol. 22, no. 2, pp. 439–449, Jun. 2007.

[27] H. Deboucha, M. Kermadi, S. Mekhilef, and S. L. Belaid, "Ultra-fast and accurate MPPT control structure for mobile PV system under fast-changing atmospheric conditions," *IEEE Trans. Sustain. Energy*, vol. 14, no. 4, pp. 2168–2176, Oct. 2023.

[28] R. Bradai et al., "Experimental assessment of new fast MPPT algorithm for PV systems under non-uniform irradiance conditions," *Appl. Energy*, vol. 199, pp. 416–429, Aug. 2017.

[29] I. G. Zurbriggen and M. Ordonez, "PV energy harvesting under extremely fast changing irradiance: State-plane direct MPPT," *IEEE Trans. Ind. Electron.*, vol. 66, no. 3, pp. 1852–1861, Mar. 2019.

[30] V. Utkin, J. Guldner, and J. Shi, *Sliding Mode Control in Electro-Mechanical Systems*, 2nd ed., Boca Raton, FL, USA: CRC Press, 2009.

[31] L. Wu, J. Liu, S. Vazquez, and S. K. Mazumder, "Sliding mode control in power converters and drives: A review," *IEEE/CAA J. Autom. Sinica*, vol. 9, no. 3, pp. 392–406, Mar. 2022.

[32] C.-C. Chu and C.-L. Chen, "Robust maximum power point tracking method for photovoltaic cells: A sliding mode control approach," *Sol. Energy*, vol. 83, no. 8, pp. 1370–1378, Aug. 2009.

[33] H.-T. Yau, C.-J. Lin, and C.-H. Wu, "Sliding mode extremum seeking control scheme based on PSO for maximum power point tracking in photovoltaic systems," *Int. J. Photoenergy*, vol. 2013, pp. 1–10, Apr. 2013.

[34] E. Bianconi et al., "A fast current-based MPPT technique employing sliding mode control," *IEEE Trans. Ind. Electron.*, vol. 60, no. 3, pp. 1168–1178, Mar. 2013.

[35] Y. Levron and D. Shmilovitz, "Maximum power point tracking employing sliding mode control," *IEEE Trans. Circuits Syst. I, Reg. Papers*, vol. 60, no. 3, pp. 724–732, Mar. 2013.

[36] C. Cabal, L. Martínez-Salamero, L. Séguier, C. Alonso, and F. Guinjoan, "Maximum power point tracking based on sliding-mode control for output-series connected converters in photovoltaic systems," *IET Power Electron.*, vol. 7, no. 4, pp. 914–923, Apr. 2014.

[37] Y. M. Alsmadi et al., "Sliding mode control of photovoltaic based power generation systems for microgrid applications," *Int. J. Control*, vol. 94, no. 6, pp. 1704–1715, Jun. 2021.

[38] O. Lopez-Santos et al., "Analysis, design, and implementation of a static conductance-based MPPT method," *IEEE Trans. Power Electron.*, vol. 34, no. 2, pp. 1960–1979, Feb. 2019.

[39] A. El Aroudi, R. Haroun, G. Zhang, P. Zheng, M. Al-Numay, and H. H. C. Iu, "Fast voltage-based MPPT control for high gain switched inductor DC–DC boost converters," in *Proc. IEEE Int. Symp. Circuits Syst. (ISCAS)*, Oct. 2020, pp. 12–14.

[40] J. A. Barrado, A. E. Aroudi, H. Valderrama-Blavi, J. Calvente, and L. Martinez-Salamero, "Analysis of a self-oscillating bidirectional DC–DC converter in battery energy storage applications," *IEEE Trans. Power Del.*, vol. 27, no. 3, pp. 1292–1300, Jul. 2012.

[41] N. Femia, G. Petrone, G. Spagnuolo, and M. Vitelli, "Optimization of perturb and observe maximum power point tracking method," *IEEE Trans. Power Electron.*, vol. 20, no. 4, pp. 963–973, Jul. 2005.

[42] M. A. Elgendy, B. Zahawi, and D. J. Atkinson, "Assessment of perturb and observe MPPT algorithm implementation techniques for PV pumping applications," *IEEE Trans. Sustain. Energy*, vol. 3, no. 1, pp. 21–33, Jan. 2012.

[43] H. Sira-Ramirez, "Sliding motions in bilinear switched networks," *IEEE Trans. Circuits Syst.*, vol. CS-34, no. 8, pp. 919–933, Aug. 1987.

[44] L. Martinez-Salamero, A. Cid-Pastor, A. E. Aroudi, R. Giral, J. Calvente, and G. Ruiz-Magaz, "Sliding-mode control of DC–DC switching converters," in *Proc. IFAC World Congr.*, Jan. 2011, vol. 44, no. 1, pp. 1910–1916.

[45] H. Sira-Ramirez, "Sliding regimes in general non-linear systems: A relative degree approach," *Int. J. Control*, vol. 50, no. 4, pp. 1487–1506, Oct. 1989.



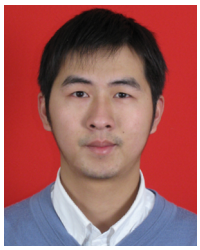
Reham Haroun (Member, IEEE) received the bachelor's degree in power and electrical engineering from Aswan Faculty of Engineering, South Valley University, Aswan, Egypt, in 2004, the master's degree from South Valley University in 2009, and the Ph.D. degree from Universitat Rovira i Virgili, Tarragona, Spain, in 2014. From 2004 to 2009, she was a Lecture Assistant at South Valley University. From 2004 to 2009, she was a member of Aswan Power Electronics Application Research Center (APEARC) Group. She works currently as Researcher at the Group of Automatic Control and Industrial Electronics (GAEI), Rovira i Virgili University. Her research interests include power electronics applications, including dc–dc switched power supplies, and ac–dc converters with power factor correction (PFC).



Abdelali El Aroudi (Senior Member, IEEE) received the bachelor's degree in physical science from the Faculté des Sciences, Université Abdelmalek Essaadi, Tetouan, Morocco, in 1995, and the Ph.D. degree (Hons.) in applied physical science from the Universitat Politè cnica de Catalunya, Barcelona, Spain, in 2000. He is currently a Full Professor with the Department of Electronics, Electrical Engineering and Automatic Control, University of Rovira i Virgili, Tarragona, Spain. His research interests include the field of dynamics, design and control of power conditioning for electric vehicles and renewable energy applications, power factor correction, and battery modeling. He was an Associate Editor of the *IET Circuits, Systems and Devices*, *IET Power Electronics*, *IET Electronics Letters*, and IEEE OPEN JOURNAL OF CIRCUITS AND SYSTEMS. He was a Guest Editor of IEEE JOURNAL ON EMERGING AND SELECTED TOPICS IN CIRCUITS AND SYSTEMS in 2015, IEEE TRANSACTIONS ON CIRCUITS AND SYSTEMS—II: EXPRESS BRIEFS in 2018, and *Energies* from 2018 to 2019. From 2019 to 2023, he was a Topic Editor of *Energies*. He currently serves as an Associate Editor for *International Journal of Circuit Theory and Applications*.



Kuntal Mandal (Member, IEEE) received the Bachelor of Engineering degree in electrical engineering from the Jalpaiguri Government Engineering College, University of North Bengal, Siliguri, West Bengal, India, in 2003, the master's degree in control system engineering from Jadavpur University, Kolkata, India, in 2006, and the Ph.D. degree in electrical engineering from IIT Kharagpur, Kharagpur, West Bengal, India, in 2013. From June 2012 to January 2017, he was a Post-Doctoral Researcher at Indian Institute of Science Education and Research Kolkata, Mohanpur, West Bengal, India, and King Abdulaziz University, Jeddah, Saudi Arabia. From February 2017 to August 2022, he was an Assistant Professor with the Department of Electrical and Electronics Engineering, National Institute of Technology Sikkim, Sikkim, India. Since September 2022, he has been working as a Beatriu de Pinós Fellow with the Grup d'Automàtica i Electrònica Industrial (GAEI), Department d'Enginyeria Electrònica, Eléctrica i Automàtica (DEEEA), Universitat Rovira i Virgili (URV), Tarragona, Spain. From May 2024 to February 2025, he also worked as an External R&D Engineer at IDIADA Automotive Technology, Santa Oliva, Tarragona. His research interests include nonlinear control and dynamics of interconnected power electronic circuits, electric vehicles, chargers, and microgrids.



Guidong Zhang (Senior Member, IEEE) was born in Shantou, Guangdong, China, in 1986. He received the B.Sc. degree from Xi'an University of Technology in 2008 and the dual Ph.D. degrees from South China University of Technology and FernUniversität, Hagen, in 2014 and 2015, respectively. From 2015 to 2016, he was a Post-Doctoral Fellow at The University of Hong Kong. He is currently a Professor with the School of Automation, Guangdong University of Technology, Guangzhou, China. He received an Endeavour Research Fellowship in Australia in 2017 and visited the University of Western Australia for half a year. He has received seven valuable scientific awards, published a Springer monograph, about 70 journal articles, and obtained 70 patents. His research interests include high-performance converter design and control, renewable energy generation, and storage. He is currently a Review Editor of *International Journal of Circuit Theory and Applications* and an Associate Editor of *Chinese Journal of Electrical Engineering* and *International Journal of Computational Intelligence Systems*.



Zhen Li (Senior Member, IEEE) received the B.Eng. and M.Eng. degrees in measurement science and control technology from Harbin Institute of Technology, Harbin, China, in 2006 and 2008, respectively, and the Ph.D. degree from The Hong Kong Polytechnic University, Hong Kong, SAR, China, in 2012.

In December 2012, he joined the School of Automation, Beijing Institute of Technology, as a Lecturer, where he is currently an Associate Professor. He was a Research Assistant/Associate at the Applied Nonlinear Circuits and System Research Group, Department of Electronic and Information Engineering, The Hong Kong Polytechnic University, from October 2011 to September 2012 and December 2013 to January 2014. His main research interests include stability analysis and control for renewable energy systems. He currently serves as an Associate Editor for IEEE TRANSACTIONS ON INTELLIGENT TRANSPORTATION SYSTEMS and Commission of Awards for IFAC Technical Committee. He was an Associate Editor of IEEE TRANSACTIONS ON CIRCUITS AND SYSTEMS—I: REGULAR PAPERS, IEEE TRANSACTIONS ON CIRCUITS AND SYSTEMS—II: EXPRESS BRIEFS, IEEE ACCESS, and a Guest Editor of IEEE JOURNAL ON EMERGING AND SELECTED TOPICS IN CIRCUIT AND SYSTEMS. He also served as the Chair for IEEE Power and Energy CAS Technical Committee.



Luis Martínez-Salamero (Life Senior Member, IEEE) received the Ingeniero de Telecomunicacion and Ph.D. degrees from the Universidad Polité cnica de Cataluna, Barcelona, Spain, in 1978 and 1984, respectively, and the Doctor Honoris Causa degree from Université Toulouse III Paul Sabatier, France, in 2024. From 1978 to 1992, he taught circuit theory, analog electronics, and power processing at the Escuela Técnica Superior de Ingenieros de Telecomunicacion, Barcelona, Spain. From 1992 to 1993, he was a Visiting Professor at the Center for Solid State Power Conditioning and Control, Department of Electrical Engineering, Duke University, Durham, NC. From 2003 to 2004, 2010 to 2011, and March 2018 to September 2018, he was a Visiting Scholar at the Laboratory of Architecture and Systems Analysis (LAAS), National Agency for Scientific Research (CNRS), Toulouse, France. Since 1995, he has been a Full Professor with the Department of Electrical, Electronic and Automatic Control Engineering, School of Electrical and Computer Engineering, Rovira i Virgili University, Tarragona, Spain, where he managed the Research Group in Automatic Control and Industrial Electronics (GAEI) from 1998 to 2018. His research interests include structure and control of power conditioning systems, namely, electrical architecture of satellites and electric vehicles, as well as nonlinear control of converters and drives, and power conditioning for renewable energy.